Understanding losses in halide perovskite thin films

Adhyaksa, G.W.P.

Publication date
2018
Document Version
Other version
License
Other

2

Carrier Diffusion Lengths in Halide Perovskites

This Chapter reports experimental values of carrier diffusion lengths in halide perovskite thin films and describes how processing, composition, aging and surface passivation affect the results. Considering the many possibilities for all three ions in the halide perovskite structure, hundreds of distinct compositions have already been reported. Such compositional changes can alter the carrier diffusion length - a key parameter for solar cell performance. Given the large compositional and processing parameter space, a rapid and simple technique for directly measuring diffusion length is needed. Here we use a laser grating technique to screen the diffusion length in perovskite materials. First, in pure $CH_3NH_3PbI_3$ we observe the diffusion length is largely dependent on the controlled processing conditions. Next, we partially replace iodide (I) with bromide (Br) and show that surprisingly, the diffusion length increases after aging for 1 month in air. Finally, we use a 4-nm Al_2O_3 layer (atomic layer deposition) to passivate the surface of $CH_3NH_3PbBr_3$, leading to a remarkable increase in diffusion length from 201 nm to 532 nm. The correlation that we have established between materials processing and diffusion length offers guidance in how to improve materials for devices.

2.1 Introduction

Hybrid halide perovskites are an emerging class of semiconductors that has drawn great interest recently because of its simple solution processing, tunable band gap,

high solar cell efficiency, and low lasing threshold [1–5]. They have the same ABX_3 configuration as the classic oxide perovskites but have metal halide rather than metal oxide corner-sharing octahedra. Typically, organic cation A is methylammonium (MA) or formamidinium (FA), B is lead (Pb) or tin (Sn), and X is chloride (Cl), bromide (Br), or iodide (I); already combining just these ions in pure or 50/50 mixes, nearly 50 distinct varieties emerge. Such compositional variations strongly affect material properties. For example, the addition of only a few percent of $PbCl_2$ to $MAPbI_3$ (known as $MAPbI_{3-x}Cl_x$) increases the film's diffusion length from ~ 100 nm to 1 μm and raises optimized photovoltaic efficiency from 4.2 % to 12.2 % [6]. Even within a single material composition, solvent engineering used to increase the domain size of the film has already been shown to have dramatic effects on device performance [3, 7]. While there are many ways to screen materials and processing conditions, the diffusion length of the photogenerated carrier has been one of the properties most strongly correlated with optoelectronic device performance [6, 8]. Despite this importance, the most common methods for measuring this diffusion length are not compatible with simple, rapid screening that would be ideal for testing the large number of possible new materials and processing conditions. For example, photoluminescence lifetime measurements can be combined with mobility measurements to yield indirectly the carrier diffusion length, but these measurements are impractically slow to be used for routine testing. Clearly a simple, rapid, and direct method for measuring diffusion length would be useful in screening both new hybrid halide perovskite materials and processing conditions that lead to better material quality.

Here we apply such a method, called the steady-state photocarrier grating (SSPG) technique, to hybrid perovskite materials and use it to investigate the influence of material composition, material processing conditions, aging, and surface passivation on the diffusion length. Originally developed in the 1980s as a way to measure diffusion length in amorphous silicon thin films, SSPG relies on a change in conductivity in the presence of an optical grating created by two interfering laser beams [9, 10]. First, we use SPPG to show that varying the solvent and processing conditions can lead to at least a factor of 2 variation in the diffusion length of methylammonium lead iodide ($CH_3NH_3PbI_3$ or $MAPbI_3$). Next we demonstrate how the diffusion length varies with halide substitution, and for each composition, how it changes with aging. Finally, we show that a thin (4-nm) passivating aluminium oxide layer can increase the diffusion length of methylammonium lead bromide ($CH_3NH_3PbBr_3$ or $MAPbBr_3$) by nearly a factor of 3, while the process of adding the same coating dramatically degrades $MAPbI_3$.

2.2 Setup

Figure 2.1a shows a schematic of the SSPG measurement setup used in this study, where we measure a small change in sample conductivity (at a given voltage) in the presence of an optical grating. The grating is created by overlapping two interfering laser beams on the sample. The measurement is conducted under illumination of I_1

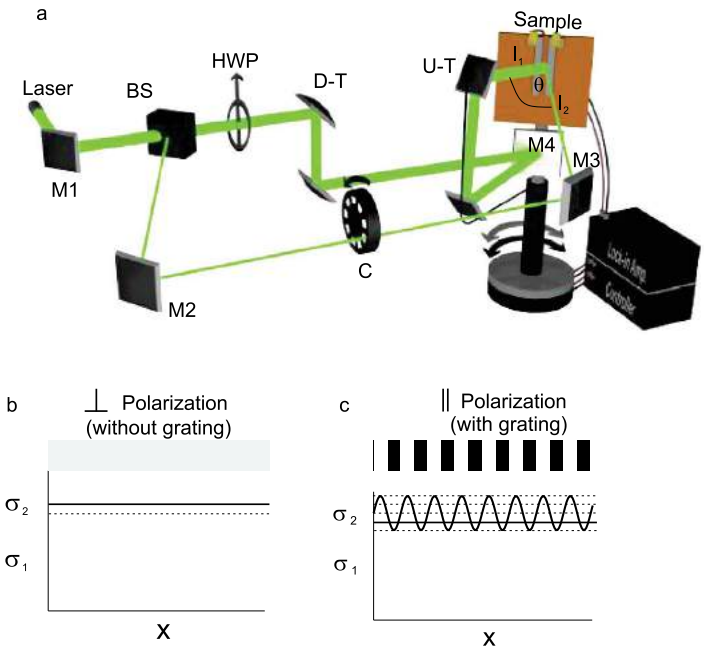

Figure 2.1: **(a)** Schematic of the setup: I_1 is the strong beam, I_2 is the weak beam, θ is the angle between I_1 and I_2, M_1, M_2, M_3, and M_4 are mirrors, BS is a beam splitter, HWP is a half-wave plate, C is chopper, U-T is up-transport mirrors, and D-T is down-transport mirrors. The axis has two rotating stages (black and gray) and each can rotate independently: (1) the sample along with M_4 underneath (gray arrow) and (2) the up-transport mirror connected with the arm (black arrow). Sample: a perovskite film deposited on a glass substrate with two coplanar gold (Au) electrodes. **(b)** Lateral conductivity pattern without grating: when I_1 and I_2 are orthogonally polarized. **(c)** Lateral conductivity with grating: when I_1 and I_2 are in parallel polarization. The conductivity σ_1 and σ_2 are not to scale for better visualization (perturbation by σ_2) should be very small relative to σ_1 in order to maintain the steady-state condition)

and I_2, where the intensity of beam I_1 is much stronger than the chopped beam I_2. In this way, I_1 serves as a background illumination ensuring an almost constant carrier generation rate over the sample surface, while I_2 acts as a probe beam providing a small perturbation ($\sim 5\%$). The change in conductivity is directly measured on the sample using a lock-in amplifier for two configurations: (1) when the two beams have orthogonal polarization states and therefore do not interfere (**Figure 2.1b**), and (2) when the polarization states are aligned, creating a periodic optical grating (**Figure 2.1c**). The grating period can be controlled by changing the angle between the two beams (grating period decreases as angle increases). The down-transport mirrors, up-transport mirrors, and rotating stages enable continuous overlap between I_1 and I_2 with varying angle.

Solving the one-dimensional steady-state diffusion equation leads to a relation

between the photoconductivity ratio and grating period [11–13]:

$$\left[\frac{1}{1-\beta}\right]^{\frac{1}{2}} = \frac{(2\pi L_D)^2}{(2Z)^{\frac{1}{2}}}\left[\frac{1}{\Lambda}\right]^2 + \frac{1}{(2Z)^{\frac{1}{2}}}, \tag{2.1}$$

where Λ is the grating period, β is the photoconductivity ratio of lock-in amplifier signals under the parallel and perpendicular polarization configurations (**Figure 2.1c,b**), L_D is the diffusion length of the photogenerated carrier, and Z is a fitting parameter related to non-ideal grating formation (e.g., due to surface scattering or poor photoconductivity). L_D describes ambipolar transport of the Coulomb-coupled electron and hole, but it will be dominated by the photogenerated carrier with the smaller diffusion length (e.g., minority carrier in a doped material). The value of β will be close to unity when diffusion length is much longer than the grating period. This case takes place when carrier diffusion significantly smears out the grating, so that the signal is the same if I_1 and I_2 create a grating (**Figure 2.1c**) or not (**Figure 2.1b**). Increasing the grating period beyond the diffusion length drastically decreases the sample conductivity, consequently decreasing β. The value of Z falls between 0 and 1 ($0 < Z < 1$; 1 is for a perfect grating) and depends on factors such as photosensitivity of the sample and grating contrast ratio [10]. The diffusion length (L_D) can be directly extracted from a linear fit of **equation 2.1**, with error bars coming from the fitting procedure (see Supporting Information for details).

2.3 Processing effect

We begin by studying the dependence of diffusion length on the sample preparation method using $MAPbI_3$. Samples were prepared by depositing thin-film hybrid perovskites on glass substrates by spin-casting from different solvents (details in the Supporting Information). On top of the film, two gold electrodes were deposited (1 mm spacing) for electrical contacts. **Figure 2.2a** shows a transform of change in conductivity ratio (β) as a function of the grating size (Λ) for $MAPbI_3$ and the corresponding diffusion lengths for each of the three processing conditions. The film processed with dimethylsolfoxide (DMSO) solvent yielded the longest diffusion length (up to 490 nm) followed by the dimethylformamide (DMF, up to 396 nm) and gamma-butyrolactone (GBL, up to 288 nm) films. The SEM images show morphological differences consistent with the measured diffusion lengths: films cast from DMSO formed large, smooth plates, while films from DMF were continuous but had a higher roughness, and those cast from GBL had the highest apparent porosity **Figure 2.2b-d**. A variety of different processing treatments including solution filtration before spin coating and toluene anti-solvent dripping also were tested and showed distinct differences in diffusion length (more details in **Figure 2.5a**). Diffusion length values we measure are similar to what has been reported using other techniques including intensity modulated photocurrent/photovoltage spectroscopy (IMPS/IMVS), photoluminescence quenching, and photoluminescence lifetime combined with mobility, where values of 100 to 1000 nm are typical, depending on preparation conditions [6, 8, 14].

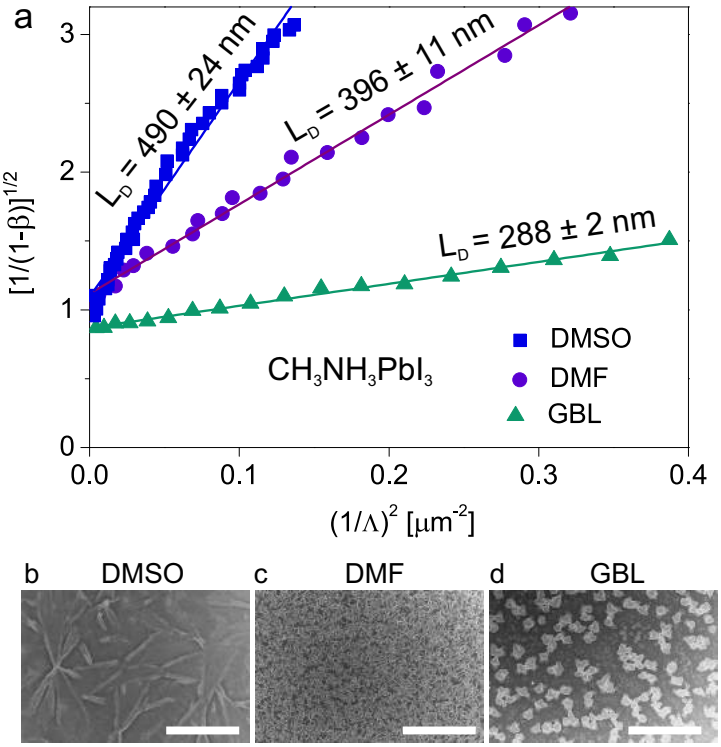

Figure 2.2: Variation of carrier diffusion length in $MAPbI_3$. **(a)** Experimental data of a transform of the photoconductivity ratio (β) as a function of grating size (Λ). The lines are the linear fitting of each corresponding experimental data set. Corresponding scanning electron microscope images of samples prepared with different solvents: **(b)** DMSO, **(c)** DMF, and **(d)** GBL.

To gain more insight into the origin of the observed morphology that is created by the solvent, we analyze X-ray diffraction patterns of six $MAPbI_3$ films processed from DMSO, DMF, and GBL, each with two different preparation conditions (**Figure 2.5b**). All films show a perovskite structure with tetragonal phase/*P4mm* (a = b = 8.86 Å, c = 12.67 Å) typical of literature reports for $MAPbI_3$ [7, 16]. We observed a direct correlation between diffusion length and the broadening of the XRD peak (**Figure 2.5c-e**), which could arise from effects such as smaller crystallite size or micro-strain within the film [17]. Assuming that the broadening arises entirely from the size of the crystallites (Supporting information for details), the full width at half-maximum of the peak corresponding to the (220) crystal orientation was used to estimate the crystallite size in the six $MAPbI_3$ films with different sample preparation conditions. The diffusion length increased by more than a factor of 2 (from 216 to 490 nm) with an increase in (XRD based) estimated crystallite size from 78 to 152 nm.

2.4 Compositional and aging effects

In addition to looking at solvent and preparation effects on diffusion length in the pure iodide, we have also examined how the diffusion length varies with halide composition. Here samples based on neat and mixed $MAPbI_3$ and $MAPbBr_3$ (hereafter denoted as $MAPb(I_{1-x}Br_x)_3$) are studied. The mixed $MAPb(I_{1-x}Br_x)_3$ is of interest because of its bandgap can be tuned throughout the region of interest for multijunction solar cells and visible light-emitting diodes or laser [2, 4, 18–22], although there are currently some problems with spontaneous phase separation under solar illumination [23]. We soaked the samples under laser illumination before the SSPG measurement in order to stabilize the properties (see methods). Spin coating from the mixed halide solutions was used to prepare these alloy samples (see methods). The bandgap gradually becomes larger by adding $MAPbBr_3$ into the neat $MAPbI_3$, as can be seen from gradual blue-shifted absorption with a clear onset following a linear relation $E_G = 0.69[Br] + 1.55$; where E_G is the optical bandgap (eV) and [Br] is the $MAPbBr_3$ fraction relative to $MAPbI_3$, from 0 to 1 (**Figure 2.6a,b**). There is only one single phase observed across the transition from tetragonal to cubic phase implying a successful incorporation of iodide-bromide ions into the perovskite structures.

The plot in **Figure 2.3a** shows that the $MAPbI_3$ film has a diffusion length (475 nm) about two times longer than that of $MAPbBr_3$ film (201 nm), as indicated by its steeper slope. All alloy compositions initially exhibit diffusion lengths below those of both pure $MAPbBr_3$ and $MAPbI_3$ (**Figure 2.3b**), consistent with an earlier proposal of trap-state formation in the mixed halide perovskites [23]. Interestingly, after aging the films for 1 month (stored in air at room temperature in the dark) all mixed halide films show a substantial increase in diffusion length from initial values of 151 - 183 nm to final values of 238 - 392 nm (**Figure 2.3b** and **Figure 2.7**). The diffusion length in aged alloy films increases proportionally with the Br fraction up to 0.66 (at 1.97 eV band gap) before dropping to values very close to those seen in the pure bromide film. The pure bromide film showed no change in diffusion length with aging, while pure iodide film showed a large decrease in diffusion length after one month. This result is consistent with the XRD, which showed partial decomposition to lead iodide only for the pure iodide perovskite; the pure bromide and mixed halide perovskite films showed no crystalline secondary phases (**Figure 2.6c**). The only change in the alloy perovskite films with aging was a slight blue shift in the absorption onset (**Figure 2.6a,b**), consistent with a previous report [20].

The origin of increased diffusion length with aging for mixed halide perovskite films is still unclear, but reactive oxygen species have been reported to play a role in deactivating defect states in the mixed halide perovskites [24, 25]. This strong difference in stability with variation in composition underlines the importance of having a simple and rapid technique for directly measuring the diffusion length of the perovskite itself, isolating its aging characteristics from those of the interfacial and contact layer used in complete devices.

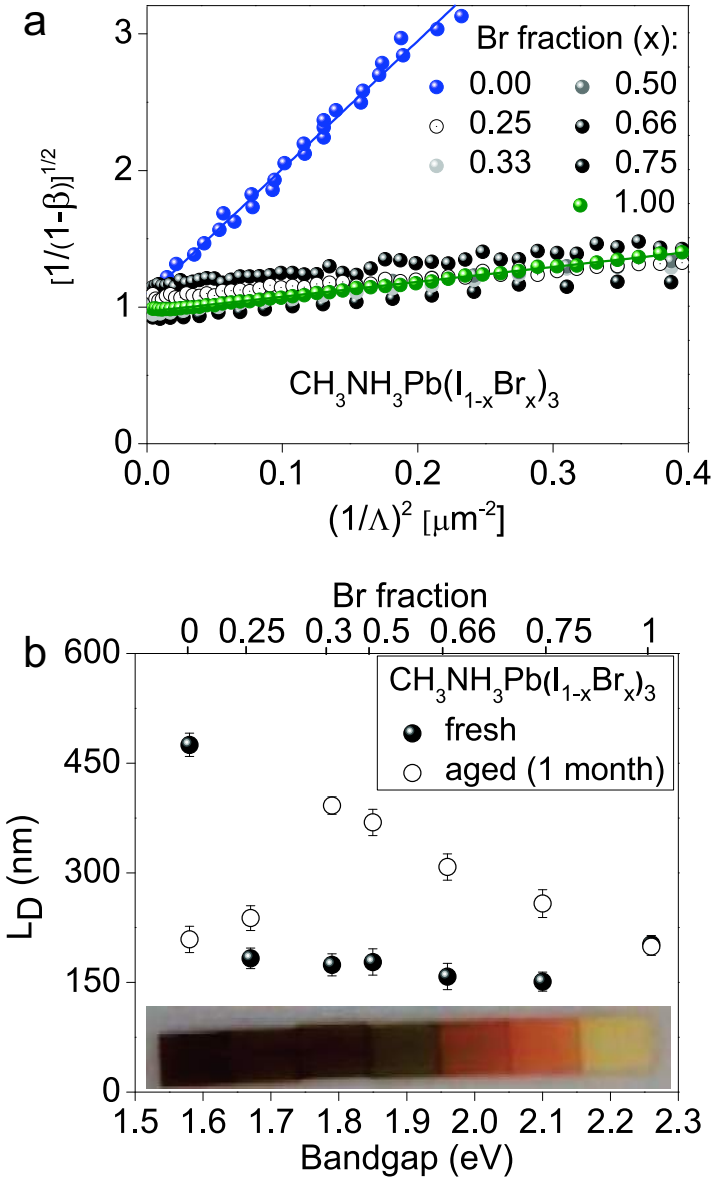

Figure 2.3: Diffusion length and aging effects in $MAPb(I_{1-x}Br_x)_3$. **(a)** Experimental data of a transform of the photoconductivity ratio β as a function of grating size (Λ) before aging. The lines are the linear fitting of data from each corresponding composition (the fitting lines and diffusion length for mixed samples are not displayed for clarity). **(b)** Diffusion length as a function of (initial) optical bandgap and bromide fraction: fresh sample (filled circle) and aged samples (open circel); inset photograph of aged samples arranged with their corresponding bandgap.

2.5 Surface passivation effect

Although the experiment creates an optical grating throughout the entire perovskite film thickness, a transfer matrix calculation [26, 27] shows that most of the highest photocarrier generation rate occurs at the surface of the film. This suggests that the SSPG technique could be sensitive to surface recombination and surface passivation effects [28]. **Figure 2.4** shows the transform of the photoconductivity ratio as a function of grating size of $MAPbI_3$ and $MAPbBr_3$ films before and after coating with a 4-nm thin amorphous aluminum oxide (Al_2O_3) layer deposited by atomic layer deposition (ALD). The deposition takes place at 100 °C using trimethylaluminum (TMA) and water (H_2O) as the Al_2O_3 precursors and the whole process takes 30 min (50 cycles). There is a dramatic increase in diffusion length for the $MAPbBr_3$ film from 201 to 532 nm, while the diffusion length of the $MAPbI_3$ film decreases from 475 to 213 nm. From XRD it is clear that $MAPbI_3$ decomposes substantially, as indicated by the appearance of PbI_2 precursor peaks (**Figure 2.10b**) after ALD deposition. In fact, we observed that the $MAPbI_3$ had started to decompose even after 10 cycles of ALD (<1 nm). This can explain both the lower diffusion length and poor signal-to-noise ratio in the measurement. In contrast, the cubic phase of $MAPbBr_3$ is still preserved without any trace of precursor peaks observed (**Figure 2.10a**).

To elucidate if surface passivation is the main reason for the diffusion length improvement, we conducted a vacuum annealing experiment by placing a $MAPbBr_3$ film in the ALD chamber in which all parameters were set to be the same (100 °C, 30 min, 10^{-3} mbar), only without feeding in the precursors. We observed the diffusion length also increased after the vacuum annealing, but only by about 20 % from its initial value, which cannot account for the nearly threefold increase seen after ALD (**Figure 2.9**). Previously a thin ALD alumina layer has been shown to be an effective passivation scheme for a variety of semiconductor surfaces (Si [29], CIGS [30], ZnO [31]) either through a field effect (fixed interfacial charges) or reduced interfacial trap state density, both of which reduce the surface recombination velocity. However, the exact role of the ALD passivation on hybrid perovskites is still under investigation. As ALD has been used in the past as an encapsulation layer to improve the stability of metal nanowire transparent electrodes [32], we expect it could also serve a similar role here.

2.6 Conclusions

In conclusion, we have performed a simple and rapid technique to screen quantitatively the diffusion length in halide perovskite thin films. This laser grating technique directly measures the diffusion length, which eliminates the need to measure lifetime and mobility separately. We demonstrate that the diffusion length halide perovskite is very sensitive with processing condition. For instance in $MAPbI_3$ films the diffusion length can be improved from 216 to 490 nm just by changing the deposition condition. We also show that the diffusion length in mixed $MAPb(I_{1-x}Br_x)_3$ films has a complex aging behavior that varies dramatically with composition: pure iodide films degrade,

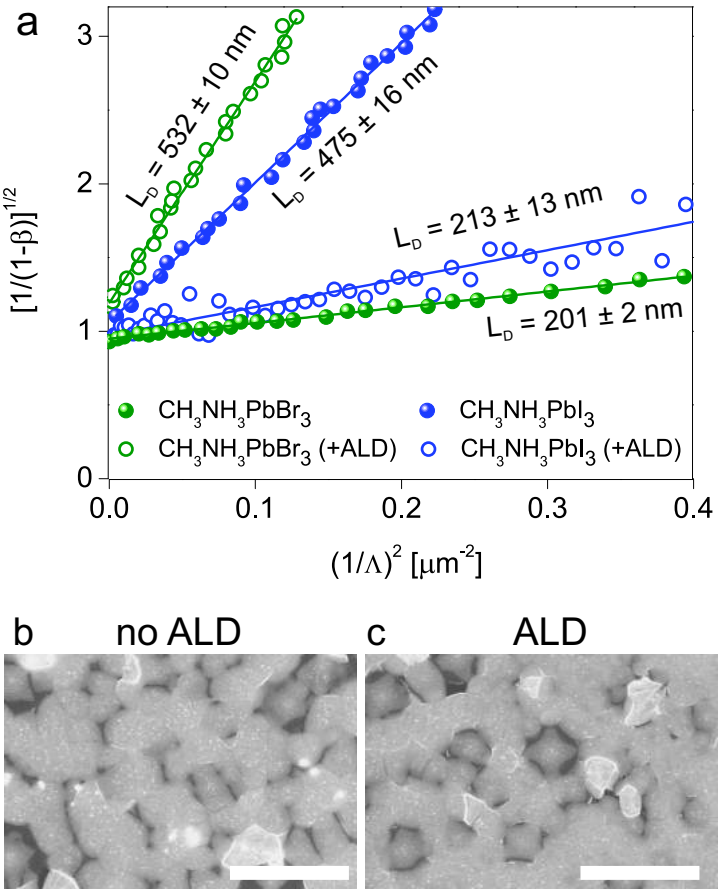

Figure 2.4: Surface passivation effect on the lateral diffusion length. **(a)** Experimental data of a transform of photoconductivity ratio (β) as a function of grating size (Λ) before and after passivation with 4-nm thin aluminum oxide film deposited by atomic layer deposition (ALD); the lines are the linear fitting of each corresponding data. Scanning electron microscope images of $MAPbBr_3$ before **(b)** and after **(c)** ALD; the bright-small dots are from sputtered chromium particles.

pure bromide films do not change, and the alloy films improve with aging. Finally, we demonstrate an improvement in the diffusion length of $MAPbBr_3$ films from 201 to 532 nm after deposition of a 4-nm thin Al_2O_3 layer by ALD. This remarkable improvement in diffusion length justifies further investigations on interfacial modification with other oxides such as nickel oxide (NiO_x), molybdenum oxide (MoO_x), and titanium oxide (TiO_x) for broadening its applicability not only for solar cells but also for photoelectrochemical water splitting.

2.7 Outlook and data validation

SSPG technique measures the change in photoconductivity laterally across the sample, which is associated with the diffusion of photogenerated carriers. This measurement geometry is distinct as compared to other methods that measure carrier diffusion through the thickness of the film. Although in a standard solar cell current is extracted in the direction perpendicular to the substrate through the thickness of the film, diffusion in the lateral direction is still strongly correlated to device efficiency for materials whose transport is not strongly anisotropic (e.g. 2D halide perovskite) or a device relying on lateral charge collection (e.g. back-contact solar cells). For example, a study of halide perovskite thin film devices with domain sizes 100 times larger than the film thickness has shown that grain boundary recombination still plays a role in decreasing solar cell performance, indicating the influence of lateral diffusion [15]. This indicates that the diffusion length measured by SSPG in the lateral geometry is a relevant parameter for solar cell performance.

In this chapter, to confirm that the SSPG technique applied to hybrid perovskites yields a diffusion length similar to that measured by more conventional techniques, we used electron beam induced current (EBIC) to measure the diffusion length in $MAPbI_3$ and $MAPbBr_3$ films of the same quality, processing conditions, and lateral sample geometry used for SSPG measurements. The EBIC values agree well with those obtained using SSPG (**Figure 2.12**). This setup has also been used to benchmark carrier diffusion lengths in halide perovskites with state-of-the-art silicon based (a-Si:H, a-SiGe:H, and μ c-Si:H), and chalcopyrite based ($Cu(In,Ga)Se_2$) thin films [33]. The next generation of the SSPG setup to account further for error corrections and beyond will be discussed in Chapter 4.

2.8 Supporting information

2.8.1 Sample preparation

Perovskite films were deposited on insulating glass substrates (1.5×1.5 cm). Prior to the deposition, the substrates were cleaned by the following protocol: 15 minutes in acetone (ultra-sonication), 15 minutes in isopropanol (ultra-sonication), 1 - 2 hours under hydrochloric acid bath (18 % in deionized water); between each step the substrates were rinsed with isopropanol and dried with nitrogen (N_2) flow; the substrates were then cleaned using an oxygen plasma (50 W, 2 minutes) to make the surface hydrophilic. The perovskite film was formed by spin-coating (10,000 rpm, for 60 seconds) a perovskite solution (1 - 2 M in DMSO, 1 M DMF, or 1 M GBL) on the glass substrate followed by thermal annealing at 100 °C for 30 minutes; all deposition processes were done in a N_2 glovebox. The perovskite solutions were prepared following the previous report [2]. It was synthesized by mixing equimolar concentrations of methylammonium halides (CH_3NH_3X; X = I, Br) and lead halide (PbX_2; X = I, Br) precursors. The mixture was ultra-sonicated to help dissolving any precursor flakes followed by 2 - 3 hours stirring in the N_2 glove box. The CH_3NH_3 was synthesized by mixing methylamine

(Sigma-Aldrich, 33 wt. % in ethanol) and hydrobromic (or hydroiodic) acid (Sigma-Aldrich, 48-57 % in H_2O) in an ice bath for 2 hours. The solvents were evaporated by heating the solution at 150 °C while stirring until a white or occasionally yellowish powder was formed. The powder was then recrystallized from a boiling ethanol to form white powders (CH_3NH_3I) or flakes (CH_3NH_3Br). The PbI_2 and $PbBr_2$ were used as purchased (Sigma-Aldrich, 99 %). For mixed $MAPb(I_{1-x}Br_x)_3$ solution, 1 M $CH_3NH_3PbI_3$ solution and 1 M $CH_3NH_3PbBr_3$ solutions were mixed by varying the volume ratio (for example 1 : 3 of I : Br means 1 mL of 1 M $CH_3NH_3PbI_3$ mixed with 3 mL of 1 M $CH_3NH_3PbBr_3$). Two co-planar gold electrodes were deposited on the thin film perovskites using a thermal evaporator (base pressure 10^{-5} mbar). The thickness of the electrodes was about 100 to 170 nm with 1 mm spacing in between. For the optimized condition: the optimized films with DMSO or GBL were from 1 M filtered solution of $MAPbI_3$ (0.22 micron, PTFE), and the solution was stirred overnight at 60 - 70 °C before the deposition. Optimized films with DMF were from 2 M solution of $MAPbI_3$, hydrochloric iodic was added into the solution (<8 % v/v), toluene drop casting during the spin-coating (at 10^{th} - 15^{th} second out of 60 seconds spinning). Otherwise, non-optimized films are from 1 M solution of $MAPbI_3$ with 60 seconds spinning with no pre-heat treatment of solution involved.

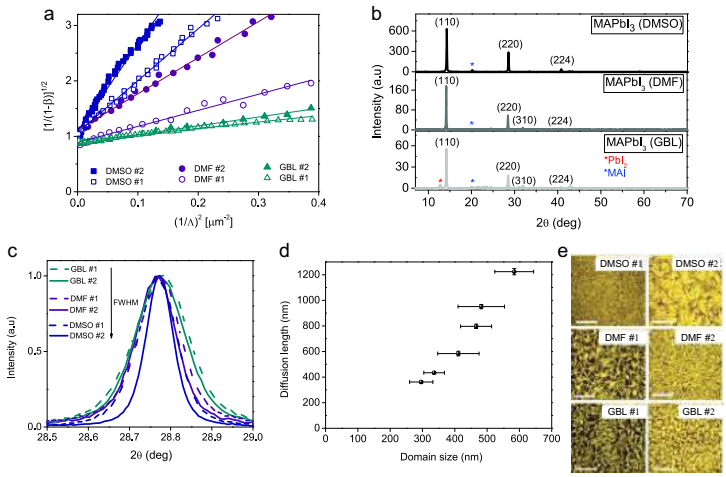

Figure 2.5: Diffusion length and crystallite size correlation in $MAPbI_3$: **(a)** Experimental data of a transform of the conductivity ratio (β) as a function of grating size (Λ): The lines are the linear fitting of each corresponding experimental data. **(b)** XRD spectra scanned from 7-70° and all showing the same crystal phase (tetragonal phase/P4mm (a = b = 8.86 Å, c = 12.67 Å) with small fraction of precursor traces (PbI_2 and MAI). **(c)** XRD at (220) crystal orientation showing different XRD peak width. **(d)** Measured diffusion length as a function of estimated crystallite size (determined from the XRD peak width). **(e)** Optical images (top view, with the scale bar of 50 μm) of samples prepared with different solvent and treatments: #1 refers to non-optimized samples, and #2 refers to the optimized ones.

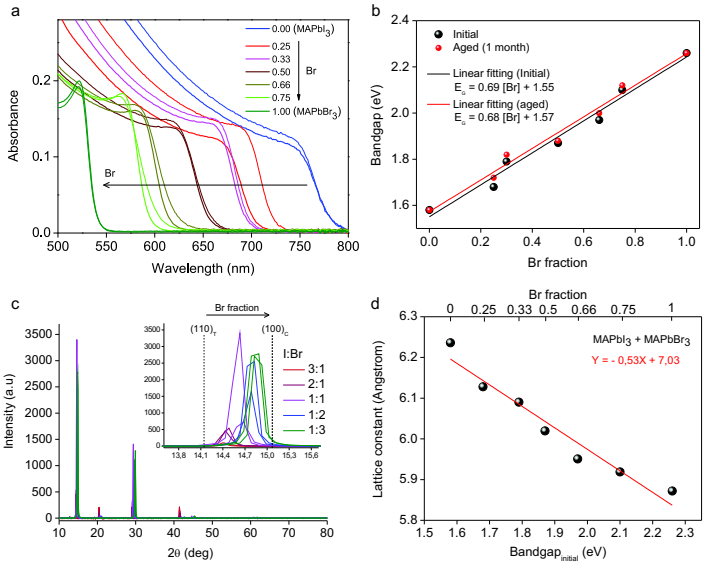

Figure 2.6: Bandgap and lattice constant correlation in $MAPb(I_{1-x}Br_x)_3$: **(a)** Absorption spectra as a function of wavelength showing a gradual blue-shift for increasing Br fraction before (thin lines) and after (thick lines) 1 month aging in air. **(b)** Linear correlation of bandgap as a function of Br fraction (bandgap increases with increasing Br fraction) showing the optical stability of $MAPb(I_{1-x}Br_x)_3$ after aging for 1 month in air. **(c)** XRD spectra showing gradual transition from (110) tetragonal to (100) cubic with increasing Br fraction. **(d)** Linear correlation of lattice constant (derived from the XRD peak) as a function of bandgap showing a linear reduction of lattice constant as the bandgap increases (as Br fraction increases).

2.8.2 Atomic layer deposition (ALD)

Al_2O_3 was deposited on the thin film of halide perovskites in an Oxford Instrument OpALTM reactor located in a cleanroom facility at Technical University of Eindhoven. The 4-nm Al_2O_3 layer, with thickness monitored by an *in situ* spectroscopic ellipsometry, were deposited on the substrate by 50 cycles at 100 °C. Each ALD cycle consists of an $Al(CH_3)_3$ dosing of 0.02 s, followed by a purge of 3.5 s, then a water vapor exposure of 0.02 s, followed by a purge of 3.5 s.

2.8.3 Laser grating setup

A diode-pumped solid-state laser (532 nm, LasNova Series 50 green) was used as an excitation source. The power output, coherence length, and polarization ratio of the laser was 4.1 mW, > 5 m, and 500 : 1, respectively. The beam was split into two-coherent beams at BK7 glass window. The intensity ratio I_1/I_2 between the two beams was 15, and adjusted by a neutral density filter. A DC voltage of 10 V was applied via the two electrodes on the sample, corresponding to an electric field strength of about 100 V/cm. This field strength was low enough to be in the diffusion regime. The polarization of beam I_1 was changed by a half-wave plate. The beam I_2 was chopped

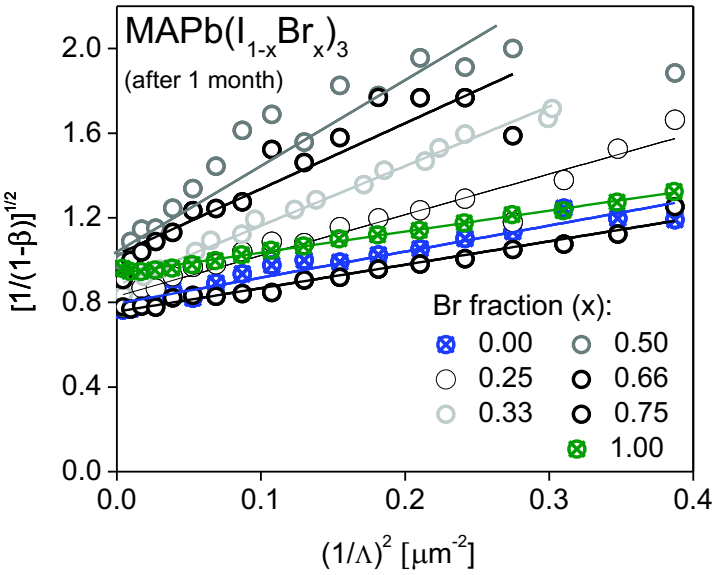

Figure 2.7: Experimental data of $MAPb(I_{1-x}Br_x)_3$ after 1 month aging (in air): Experimental data of a transform of the conductivity ratio (β) as a function of grating size (Λ), the lines are linear fittings of each corresponding experimental data. Diffusion length values and errors are tabulated in **Table S1**.

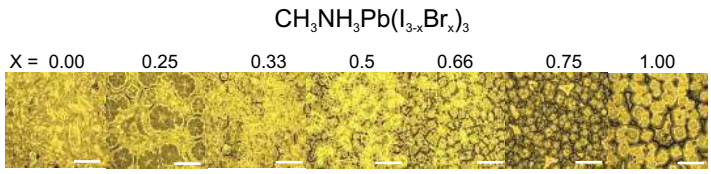

Figure 2.8: Optical images of $MAPb(I_{1-x}Br_x)_3$ after 1 month aging (in air).

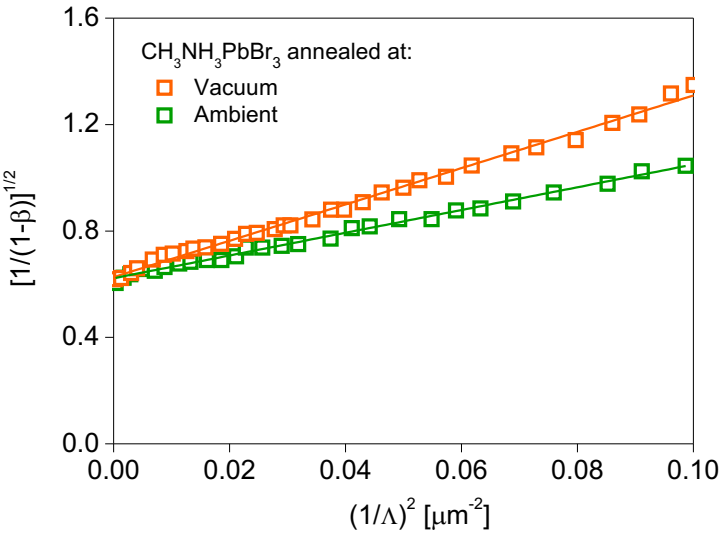

Figure 2.9: Diffusion length of MAPbBr3 under different annealing.

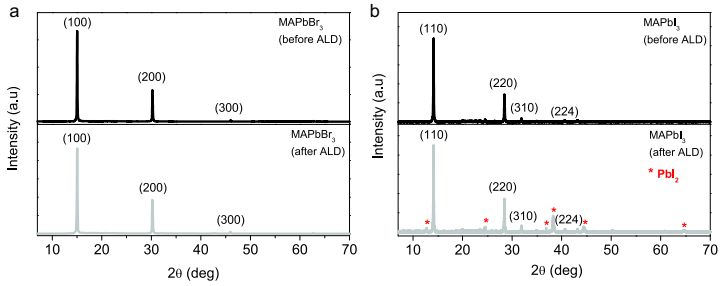

Figure 2.10: X-ray diffraction after ALD passivation.

at 110 Hz. Two rotating mirrors were used to direct the two beams onto the sample aiming for continuous overlap while changing the angle between the two-interfering beams. For hybrid perovskite measurements, To be in the linear regime, we typically varied the angle from 3° to 15°, and this corresponds to optical grating periods from ~ 5 μm down to ~ 0.8 μm; the lower boundary for the measured diffusion length is about 0.1 times the grating period. The sample was pre-soaked under ~ 100 mW/cm^2 laser illumination for 1 - 2 minutes before the measurement to minimize the light-induced phase separation effect to ensure consistent measurements.

The uncertainty of the measured diffusion length values in this chapter is derived from the linear fitting of the data to the equation 2.1. With a linear fitting of [Y] = a[X] + c; where a is the slope, and c is the intercept of the data plot. So, we can calculate the diffusion length as:

$$L_D = \frac{1}{2\pi}\left(\frac{a}{c}\right)^{\frac{1}{2}}, \tag{2.2}$$

The error bar of L_D is calculated by summing the error propagation of the slope (a) and the intercept (c) as:

$$\delta L_D = \frac{1}{4\pi}\left(\frac{a}{c}\right)^{\frac{1}{2}}\sqrt{\left(\frac{\delta a}{a}\right)^2+\left(\frac{\delta c}{c}\right)^2}, \tag{2.3}$$

The δa and δc are errors based on confidence intervals on a and c. The standard error values of a and c from the regression analysis are used to construct δa and δc. Here we take 90 % critical values from the t-distribution with 20 to 30 degrees of freedom. This gives 90 % confidence intervals that are 1.31 to 1.33 times larger than the standard error values. Further correction and considereation of data and error analysis will be discussed in Chapter 4.

2.8.4 Estimating crystallite size using X-ray diffraction analysis

The crystal structure of the samples was analyzed based on their X-ray diffraction spectra (using a Bruker D2-phaser instrument, Bragg-Brentano geometry) under the θ - 2θ configuration. The average crystallite size was determined using the Scherrer

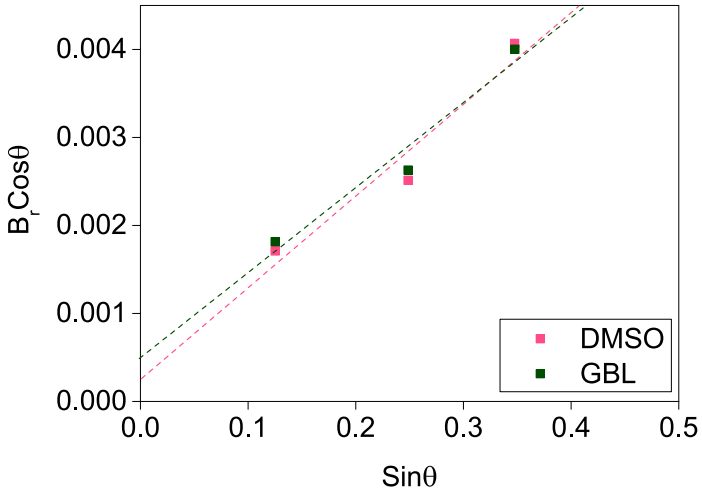

Figure 2.11: Distinguishing lattice strain and crystallite size from the XRD peak broadening. This data already substracted by the intrumental broadening.

equation [17]:

$$\langle R \rangle = \frac{k\lambda}{B\cos\theta}, \tag{2.4}$$

where $\langle R \rangle$ is the average crystallite size in the crystal direction along the normal of the diffraction plane, k is a constant that depends on the crystallite shape, but normally is approximately 0.94 ($k = 0.94$ for a cubic crystallite shape), λ is the X-ray wavelength (here $\lambda = 0.154$ nm for Cu-Kα), B is the 2θ full-width-half-maximum (FWHM) peak (in Radian) after correction by the FWHM contributed by the instrumental broadening, θ is the Bragg angle. The FWHM correction was done by taking the XRD spectra of a certified Corundum standard and substracting the XRD FWHM peak of the perovskite at 28.8° (220) with the Corundum FWHM peak at 25.6 °. A systematic error because of a different sample thickness (Z-height error correction) is minimized by scanning XRD spectra of a sample also containing CeO_2, and then adjusting the peak position according to the pure CeO_2 standard. The error range of the $\langle R \rangle$ for each sample was estimated by calculating the $\langle R \rangle$ on 3 - 4 samples with the same preparation condition. All measurements were performed under the same instrumental setting: using 0.6 divergence slit to control illuminated area, 1 mm beam knife to limit unwanted scattering and optimize the low angle spectra, nickel filter to reduce 20 - 30 % contribution from Cu-Kβ. The scan interval ($\Delta 2\theta$) was 0.01° with multiple scans repeated to improve signal-to-noise ratio.

However, the broadening of the XRD peaks is not only due to crystallite size and instrumental effects, but also lattice strain. The effect of lattice strain can be represented by the [17]:

$$B_{strain} = \eta \tan\theta, \tag{2.5}$$

where η is the strain of the perovskite material. So, the total broadening of XRD peak,

after substrating with the contribution from intrumental broadening, can be expressed as summation of equation 2.4 and 2.5:

$$B_{total} = \frac{k\lambda}{\langle R \rangle \cos\theta} + \eta \tan\theta, \tag{2.6}$$

by multiplying equation 2.6 by $\cos\theta$, we find:

$$B_{total} \cos\theta = \frac{k\lambda}{\langle R \rangle} + \eta \sin\theta, \tag{2.7}$$

If we plot the B_{total} *versus* $\sin\theta$, the intercept tells us about crystallite size, and the slope provides the strain information. The closer the intercept to the origin point (0,0), the larger the crystallite size. While the steeper the slope, the larger the strain. **Figure 2.11** shows the plot of two extrema cases used in this study (sample with largest and smallest estimated crystallite size made by DMSO, and GBL, respectively). After correction with the lattice strain, the estimated crystallite size seems to increase proportionally from the original value (equation 2.4). Although we should question the accuracy of lattice strain contribution based on this data where the second data are quite off from the linear fitting. The other way to find the strain contribution is by comparing the data with a large single crystal halide perovskite materials. However, even using a large crystal halide perovskite still gives twice larger broadening than just a Corrundum standard based on the identical intrumental setting. Unless a good standard peaks for each of the perovskite peaks (close to the actual XRD peak) is used, then doing the strain calculation artificially enlarges the calculated crystallite size and provide a larger error than just leaving out the strain calculation entirely. Therefore, we excludes the contribution of lattice strain to estimate the crystallite size in correlation with the diffusion length result.

2.8.5 Electron beam induced current (EBIC)

The samples for the EBIC measurement were prepared by depositing halide perovskite films on metal electrodes. Gold (Au) and Titanium (Ti) fingers with 2 mm spacing in between them were fabricated using two steps of photolithography. The procedure of thin-film deposition was the same as that used to prepare the films for the optical grating measurement (see sample preparation protocol). The contacts were wire-bonded to a printed circuit board, allowing the current of the perovskite films to be measured inside the SEM. The SEM used for the imaging is FEI Verios 460. The EBIC measurement was performed in the SEM as used for imaging, equipped with a current amplifier (FEMTO, DLPCA-200, gain set to ~10^{11} - 10^{9} V/A), and the electron beam was set at 10kV, 10pA, 1 ms integration time. To roughly estimate the electron trajectory, therefore interaction volume, for the given electron beam parameters entering our structure, we used a Monte Carlo simulation of the electron's trajectory (CASINO) in the solid with 10^{6} simulated electron [34]. To extract the photcurrent decay curves, the periodic noise from the EBIC maps was removed by filtering the image in Fourier space, and the current decay profiles over a uniform region of the image were averaged.

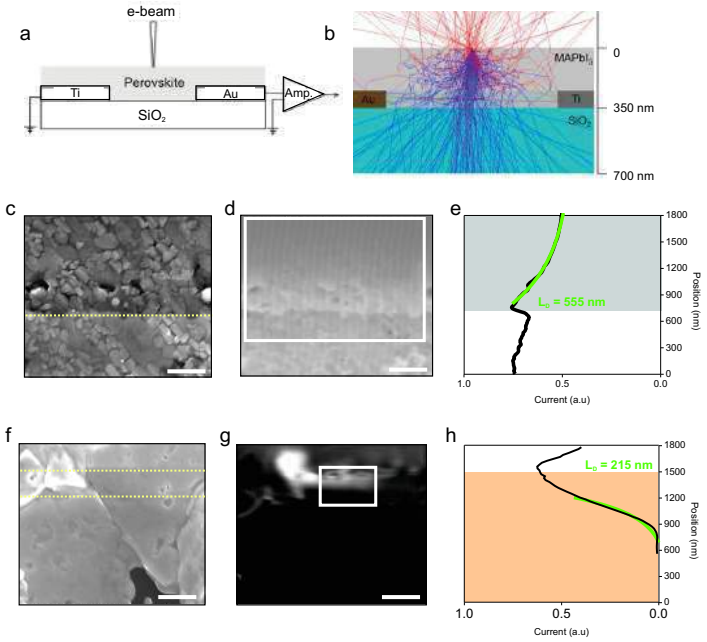

Figure 2.12: Electron beam induced current (EBIC) on $MAPbI_3$ and $MAPbBr_3$ films: **(a)** Measurement geometry. **(b)** Simulated electron trajectories and scattering events of the corresponding geometry in **figure 2.12a** (blue: secondary electron path; red: back-scattered electron path). **(c)** SEM image showing $MAPbI_3$ films on top of Au (bottom side; below the blue dashed-line) and Ti (beyond the top of the frame) contacts. **(d)** Corresponding EBIC image of **figure 2.12c**: darker areas indicate lower current; the scale bar for **figure 2.12c-d** is 400 nm. **(e)** Averaged current response profile from the EBIC extracted from **figure 2.12d** (framed with white line) showing an exponential decay tail toward the Ti side (gray area) of the depletion region (the green line is the fitting curve from which the diffusion length is obtained; L_D = 555 nm). **(f)** SEM image showing $MAPbBr_3$ films on top of Au (bottom side; below the bottom blue dashed-line) and Ti (top side; above the top blue dashed-line) contacts. **(g)** Corresponding EBIC image of **figure 2.12f**: darker areas indicated lower current; the scale bar for **figure 2.12f-g** is 2 μm. **(h)** Averaged current response profile from the EBIC extracted from **figure 2.12g** (framed with white line) showing an exponential decay tail toward the Au side (orange area) of the depletion region (the green line is the fitting curve from which the diffusion length is obtained; L_D = 215 nm).

For the $MAPbI_3$ EBIC images, this region was typically the whole frame, while for the $MAPbBr_3$ EBIC images, smaller areas were used because of non-uniformity in the morphology of the film and charging effects.

To validate our SSPG measurements, we compared the diffusion lengths determined using the SSPG technique to diffusion lengths measured using EBIC, which is a well-established technique that also measures lateral diffusion length. EBIC measurements, however, measure only local diffusion length (nm to μm scale), while SSPG measurements average over the entire film (mm scale).

According to our EBIC measurements, the diffusion lengths obtained from the current decay profiles in $MAPbI_3$ are 555 nm (**Figure 2.12e**), 512 nm, 454 nm, 518

nm, and 371 nm, as compared to the 490 ± 24 nm measured by the SSPG technique. This range of extracted diffusion length values likely originated from a local difference in crystallinity and film morphology. For the $MAPbBr_3$, EBIC-measured diffusion lengths included 215 nm (**Figure 2.12f-h**), 164 nm, 219 nm, 128 nm, 172 nm, 186 nm, and 318 nm, as compared to 201 ± 2 nm measured using SSPG. The average values (491 nm and 200 nm for $MAPbI_3$ and $MAPbBr_3$, respectively). For EBIC, the standard deviation is much larger (62 nm and 56 nm for $MAPb_3$, and $MAPbBr_3$, resepectively), as expected, because of the more local nature of the EBIC measurement. Since EBIC is a well-established technique, these measurements confirm that SSPG provides an accurate measurement of the film's lateral diffusion length averaged over a large scale.

In our EBIC measurements, we needed a relatively high voltage (10 kV) and current (50 pA) to measure a clear EBIC signal. This voltage ensures that the electron beam penetration depth is sufficient for the back electrodes can collect the signal (**Figure 2.12b**). We are aware that others have advocated using a lower voltage (1 - 3 kV) to prevent film damage over time for halide perovskite [35], but we did not see visible damage to our films with repeated scans. The instability reported in the literature could arise from the film's being damaged by preparing the cross section or from the use of transporting layer (e.g Spiro-OMeTAD) in the device. In our case, to give a structure comparable to that used for the SSPG measurements, we did not use any transporting layer, relaying on the barrier between the metal contact and the perovskite to produce a Schottky contact at which to measure th photocurrent's decay.

References

[1] M. M. Lee, J. Teuscher, T. Miyasaka, T. N. Murakami, and H. .J. Snaith, *Efficient hybrid solar cells based on meso-superstructured organometal halide perovskites*, Science **338**, 643 (2012).

[2] J. H. Noh, S. H. Im, J. H. Hoe, T. N. Mandal, and S. I. Soek, *Chemical management for colorful, efficient, and stable inorganic- organic hybrid nanostructured solar cells*, Nano Lett. **13**, 1764 (2013).

[3] N. J. Jeon, J. H. Noh, W. S. Yang, Y. C Kim, S. Ryu, J. Seo, and S. I. Soek, *Compositional engineering of perovskite materials for high- performance solar cells*, Nature **517**, 476 (2015).

[4] H. Zhu, Y. Fu, F. Meng, X. Wu, Z. Gong, Q. Ding, M. V. Gustafsson, M. T. Trinh, S. Jin, and X. Y. Zhu, *Lead halide perovskite nanowire lasers with low lasing thresholds and high quality factors*, Nat. Mater. **14**, 636 (2015).

[5] J. Burschka, N. Pellet, S. J. Moon, R. Humphry-Baker, P. Gao, M. K. Nazeeruddin, and M. K. Grätzel, *Sequential deposition as a route to high-performance perovskite-sensitized solar cells*, Nature **499**, 316 (2013).

[6] S. D. Stranks, G. E. Eperon, G. Grancini, C. Menelaou, M. J. P. Alcocer, T. Leijtens, L. M. Herz, A. Petrozza, and H. J. Snaith, *Electron-hole diffusion lengths exceeding 1 micrometer in an organometal trihalide perovskite absorber*, Science **342**, 341 (2013).

[7] N. J. Jeon, J. H. Noh, Y. C. Kim, W. S. Yang, S. Ryu, and S. I. Seok, *Solvent engineering for high-performance inorganic-organic hybrid perovskite solar cells*, Nat.Mater. **13**, 897 (2014).

[8] G. Xing, N. Mathews, N. Sun, S. S. Lim, Y. M. Lam, M. Grätzel, S. Mhaisalkar, and T. C. Sum, *Long-range balanced electron-and hole- transport lengths in organic-inorganic* $CH_3NH_3PbI_3$, Science **342**, 344 (2013).

[9] S. Komuro, Y. Aoyagi, Y. Segawa, S. Namba, A. Masuyama, H. Okamoto, and Y. Hamakawa, *Study of optically induced degradation of conductivity in hydrogeneted amorphous silicon by transient grating method*, Appl. Phys. Lett. **42**, 807 (1983).

[10] D. Ritter, E. Zeldov, K. Weiser, *Steady-state photocarrier grating technique for diffusion length measurement in photo- conductive insulators*, Appl. Phys. Lett. **53**, 992 (1988).

[11] I. Balberg, A. E. Delahoy, and H. A. Weakliem, *Ambipolar diffusion length measurements on hydrogenated amorphous silicon p- i -n structures*, App. Phys. Let. **53**,1949 (1988).

[12] J. P. Nicholson, *Fresnel corrections to measurements of ambipolar diffusion length*, J. Appl. Phys. **88**, 4693 (2000).

[13] K. Hattori, H. Okamoto, and Y. Hamakawa, *Theory of the steady- state-photocarrier-grating technique for obtaining accurate diffusion- length measurements in amorphous silicon*, Phys. Rev. B: Condens. Matter Mater. Phys. **45**, 1126 (1992).

[14] J. H. Hoe, D. H. Song, H. J. Han, S. Y. Kim, D. Kim, H. Kim, T. K. Shin, T. K. Ahn, C. Wolf, T. W. Lee, and S. H. Im, *Planar $CH_3NH_3PbI_3$ perovskite solar cells with constant 17.2% average power conversion efficiency irrespective of the scan rate*, Adv. Mater. **27**, 3424 (2015).

[15] Y. Yang, Y. Han, M. Yang, S. Choi, K. Zhu, J. M. Luther, and M. C. Beard, *Low surface recombination velocity in solution-grown $CH_3NH_3PbBr_3$ perovskite single crystal*, Nat. Commun. **6**, 7961 (2015).

[16] C. Quarti, E. Mosconi, J. M. Ball, V. D. Innocenzo, C. Tao, S. Pathak, H. J. Snaith, A. Petrozza, and F. De Angelis, *Structural and optical properties of methylamaonium lead iodide across the tetragonal to cubic phase transition: implications for perovskite solar cells*, Energy Environ. Sci. **9**, 155 (2016).

[17] C. Suryanarayana and M. G. Norton, *X-ray diffraction: a practical approach*, Plenum Press, New York, 1998.

[18] T. P. White, N. N. Lai, and K. R. Catchpole, *Tandem solar cells based on high-efficiency c-Si bottom cells: top cell requirements for > 30% efficiency*, IEEE J. Photovolt. **4**, 208 (2014).

[19] L. Gil-Escrig, A. Miquel-Sempere, M. Sessolo, and H. J. Bolink, *Mixed iodide-bromide methylammonium lead perovskite-based diodes for light emission and photovoltaics*, J. Phys. Chem. Lett. **6**, 3743 (2015).

[20] A. Sadhanala, F. Deschler, T. H. Thomas, S. E. Dutton, K. C. Goedel, F. C. Hanusch, M. Lai, U. Steiner, T. Bein, P. Docampo, D. Cahen, and R. H. Friend, *Preparation of single-phase films of $CH_3NH_3Pb(I_{1-x}Br_x)_3$ with sharp optical band edges*, J. Phys. Chem. Lett. **6**, 3743 (2015).

[21] S. A. Kulkarni, T. Baikie, P. P. Boix, N. Yantara, N. Mathews, and S. Mhaisalkar, *Band-gap tuning of lead halide perovskites using a sequential deposition process*, J. Mater. Chem. A **2**, 9221 (2014).

[22] H. Cho, S. -H. Jeong, M. -H. Park, Y. -H. Kim, C. Wolf, C. -L. Lee, J. H. Hoe, A. Sadhanala, N. Myoung, S. Yoo, S. H. Im, R. H. Friend, and T. -W. Lee, *Overcoming the electroluminescence efficiency limitations of perovskite light-emitting diodes*, Science A **350**, 1222 (2015).

[23] E. T. Hoke, D. J. Slotcavage, E. R. Dohner, A. R. Bowring, H. I. Karunadasa, and M. D. McGehee, *Reversible photo-induced trap formation in mixed-halide hybrid perovskites for photovoltaics*, Chem. Sci. **6**, 613 (2015).

[24] Y. Tian, M. Peter, E. Unger, M. Abdellah, K. Zheng, T. Pullerits, A. Yartsev, V. Sundstrom, and I. G. Scheblykin, *Mechanistic insights into perovskite photoluminescence enhancement: light curing with oxygen can boost yield thousandfold*, Phys. Chem. Chem. Phys. **17**, 24978 (2015).

[25] J. F. Galisteo-Lopez, M. Anaya, M. E. Calvo, and H. Miguez, *Environmental effects on the photophysics of organic-inorganic halide perovskites*, J. Phys. Chem. Lett. **6**, 2200 (2015).

[26] P. Peumans, A. Yakimov, and S. R. Forrest, *Small molecular weight organic thin-film photodetectors and solar cells*, J. Appl. Phys. **93**, 3693 (2003).

[27] G. F. Burkhard, E. T. Hoke, and M. D. McGehee, *Accounting for intergerence, scattering, and electrode absorption to make accurate internal quantum efficiency measurement in organic and other thin solar cells*, Adv. Mater. **22**, 3293 (2010).

[28] M. Haridim, K. Weiser, and H. Mell, *Use of the steady-state photocarrier-grating technique for the study of the surface recombination velocity of photocarriers and the homogeneity of hydrogenated amorphous silicon films*, Philos. Mag. B **67**, 171 (1993).

[29] S. Kato, Y. Kurokawa, S. Miyajima, Y. Watanabe, A. Yamada, Y. Ohta, Y. Niwa, and M. Hirota, *Improvement of carrier diffusion length in silicon nanowire arrays using atomic layer deposition*, Nanoscale Res. Lett. **8**, 361 (2013).

[30] B. Vermang, V. Fjallstrom, X. Gao, and M. Edoff, *Improved rear surface passivation of Cu(In,Ga)Se_2 solar cells: a combination of an Al_2O_3 rear surface passivation layer and nanosized local rear point contacts*, Nanoscale Res. Lett. **8**, 361 (2013).

[31] M. Law, L. E. Greene, A. Radenovic, T. Kuykendall, J. Liphardt, and P. Yang, *ZnO-Al_2O_3 and ZnO-TiO_2 core-shell nanowire dye- sensitized solar cells*, J. Phys. Chem. B **110**, 22652 (2006).

[32] P. -C. Hsu, H. Wu, T. J. Carney, M. T. McDowell, Y. Yang, E. C. Garnett, M. Li, L. Hu, and Y. Cui, *Passivation coating on electrospun copper nanofibers for stable transparent electrodes*, ACS Nano **6**, 5150 (2012).

[33] L. W. Veldhuizen, G. W. P. Adhyaksa, M. Theelen, E. C. Garnett, and R. E. I. Schropp, *Benchmarking photoactive thin-film materials using a laser-induced steady-state photocarrier grating*, Prog. Photovolt: Res. Appl. **25**, 605 (2017).

[34] H. N. Demers, N. Poirier-Demers, A. R. Couture, D. Joly, M. Guilmain, N. de Jonge, and D. Drouin, *Three-dimensional electron microscopy simulation with the CASINO Monte Carlo software*, Scanning. **33**, 92 (2011).

[35] H. Yuan, E. Debroye, K. Janssen, H. Naiki, C. Steuwe, G. Lu, M. Moris, E. Origiu, H. Uji, F. D. Schryver, P. Samori, J. Hofkens, and M. Roeffaers, *Degradation of methylammonium lead iodide perovskite structures through light and electron beam driven ion migration*, J. Phys. Chem. Lett. **7**, 561 (2016).